Received July 28, 2020, accepted August 18, 2020, date of publication August 28, 2020, date of current version September 24, 2020.

Digital Object Identifier 10.1109/ACCESS.2020.3020247

A Fast and Reliable Three-Dimensional Centerline Tracing: Application to Virtual Cochlear Implant Surgery

MAJID ZAMANI[1], (Member, IEEE), ENVER SALKIM[1], (Member, IEEE), SHAKEEL R. SAEED[2], AND ANDREAS DEMOSTHENOUS[1], (Fellow, IEEE)

[1]Department of Electronic and Electrical Engineering, University College London (UCL), London WC1E 7JE, U.K.
[2]UCL Ear Institute, London WC1X 8EE, U.K.

Corresponding author: Andreas Demosthenous (a.demosthenous@ucl.ac.uk)

This work was supported by UCL Innovation and Enterprise with funding from the Engineering and Physical Sciences Research Council under Grant EP/R511638/1.

ABSTRACT This paper presents a rapid and unsupervised three-dimensional (3D) tubular structure tracing algorithm for the detection of safe trajectories in cochlear surgery. The algorithm utilizes a generalized 3D cylinder model which offers low-order parameterization, enabling low-cost recursive directional tubular boundary analysis and derivation of tubular statistics (i.e. centerline coordinates). Unlike previous work, the proposed algorithm circumvents excessive computation per voxel while enhancing angular centerline traversing efficiency which is critical in cochlear implant surgery navigation. To accomplish this, design considerations include: 1) accurate engineering of kernels used for border analysis, 2) modifying decision-making in identifying optimal tracing angle with homogeneity criterion, 3) reducing tubular change exploratory search cost through discrete convolution analysis, and 4) a cross-section calibration engine which suppresses centerline angular deviations as well as recording a history of geometrical changes while tracing. When evaluated on synthetic imagery mimicking cochlea structural complexity and real reconstructed cochlea models, it consistently produced accurate estimates of centerline coordinates and widths-heights in the presence of noise and spatial artefacts. Validation has shown that the centerline error for the proposed algorithm is below 6 pixels and the average traced pixel performance is 92.9% of the true centerline pixels on the examined cochlea models. By restricting the image analysis to the regions of interest, the proposed algorithm performs rapid centerline tracing of the cochlea needed for real-time surgery (0.48 seconds per electrode insertion).

INDEX TERMS Automated insertion, cochlea, cross-section calibration, directional convolution, minimally invasive surgery, real-time systems, robust centerline tracing, tubular structures, virtual surgery.

I. INTRODUCTION

In most cases of sensorineural hearing loss, the primary site of functional loss resides within the hair cells of the cochlea, which results in insufficient transduction of acoustic signals into neural impulses at the auditory nerve. The spiral ganglion cells and their auditory neurons are often intact and functional but do not receive adequate stimulation from the cochlear hair cells. Cochlear implants [1], [2] can be utilized to bypass the deficient part of the auditory system, and provide direct stimulation of the auditory nerve [3], [4]. One of the most critical factors in cochlear implant surgery, where an electrode array is inserted into the scala tympani, is associated with diameter and height variations of the cochlea in which the three spiral turns dramatically change, and therefore impose geometrical limitations on the cochlear implant surgery. For example, the mean heights at the basal, middle and apical turns are 2.1 mm, 1.2 mm and 0.6 mm respectively [5]. Usually the control of optimal electrode array insertion is left to the surgeon who must define some points on the path manually using three orthogonal views. However, marking the optimal surgery path for complex tubular structures is a tedious task and increases the risk of damaging critical fine structures in the cochlea by inadvertently crossing the anatomical boundaries of the scala tympani. To avoid adverse consequences as a result of the extreme geometrical limitations, computer-assisted surgery [6] is used to identify the precise centerline trajectory inside a three-dimensional (3D) reconstructed cochlea as priori knowledge for cochlear implant electrode array insertion by

The associate editor coordinating the review of this manuscript and approving it for publication was Li He.

automatic means. This work focuses on proposing a novel and automated three-dimensional (3D) tracing algorithm of tubular structures, reducing the need for human intervention.

The rest of the paper is organized as follows. In Section II, some of the algorithms previously presented for 3D centerline tracing are briefly discussed. The design of convolution kernels is described in Section III. Section IV presents the proposed tracing algorithm and explains its building blocks including optimal tracing angle estimation, discrete jump-ahead search and calibration engine. This section also outlines other tracing algorithms for comparison. Section V presents the results of the tests on the synthetic and real 3D cochlea models using the proposed and the other tracing algorithms. Concluding remarks and discussion are provided in Section VI.

II. RELATED BACKGROUND

There are a variety of approaches that can be utilized to identify the centerline of tubular structures. One category consists of skeletonization approaches [7] and those using multiscale enhancement, morphological reconstruction and segmentation methods [8]–[11]. They require the processing of full 3D volume and every image pixel with numerous operations per pixel.

A second category tracks the centerline based on a filter or an assumed model. Commonly used filters are based on eigen-structure of the local Hessian [12], idealized tubular models of vessels [13] and Hough transforms [14] to locate vessel direction and its cross vectors at a reference frame. For example, Hessian of the image is interpreted as second order partial derivatives of 3D sub-images at reference nodes which requires extensive computation time. Cylindroidal superellipsoids [15] is a sophisticated model of probing for 3D tubular shapes using recursive fitting methods. Although the fitting-based approaches behave well across morphological complexities, they derive model parameters using maximum likelihood which is an extremely complex and lengthy process.

A third category utilizes the vectorization algorithm [16]–[19] for tubular structure boundary analysis and centerline tracing where only pixels close to the border are processed and are well-suited to real-time and robust tracing in large image sets. The sparse exploration of the boundaries yields low computational overhead but also introduces higher sensitivity to the discontinuities and geometrical complexities. An algorithm utilizing vectorization approach to handle 3D (volumetric) data is investigated in [20]. It is a fully automatic 3D neuron tracing algorithm emulating a 3D cylinder model and recursively explores the neuron topology. The simulations using the 3D cylinder algorithm on constructed cochlea models (explained in Section V) illustrate that the centerline tracing does not perform reliably when faced with high-order tubular changes. The application of the algorithm was restricted to examination by dendritic centerline tracing, which exhibited almost straight-line morphology with little deviation and was limited to simple cases.

Machine learning also offers an alternative category to identify and trace the central coordinates [21]–[23]. Steerable features and randomized decision trees are used in [21] to perform centerline extraction by learning the structural patterns of a tubular-like object. The approach in [23] uses orientation flow field and classifier to extract blood vessel centerlines. The average computation for tracing all coronaries takes about 1 minute on an Intel Core i7 2.8 GHz processor and 32 GB RAM as reported in [23].

Convolutional neural networks (CNNs) are a class of deep learning algorithms that have recently been utilized in 3D tubular structures tracing [24]–[26]. In [24], a 3D dilated CNN [27] is trained to predict the most likely direction and radius of an artery at any given seed point. The overall tracing scheme in [24] is developed based on determining a posterior probability distribution over a discrete set of possible directions as well as an estimate of the radius. The issue with this design is that the optimal direction determination is posed as a classification problem, so the possible directions are distributed on a sphere where each point corresponds to a class. The best classification performance was obtained for the directions {500, 1000 or 2000}. The design in [24] demands excessive computational cost in classifying directions and is not suitable for real-time applications (i.e. requires 20 seconds fully automatic coronary tree extraction using Nvidia Titan Xp GPU). Also, [25] and [26] proposed 3D CNNs to trace the cardiovascular tree structure. They require 58 and 25 seconds using 12GB GPU and Tesla P40 GPU respectively.

The proposed algorithm in this work is inspired by the design in [20]. It features a reliable approach to identifying the optimal tracing angle, a discrete self-exploratory boundary analysis for monitoring tubular changes, and a calibration engine to regulate centerline coordinates in case of unwanted angular deviations. It has deformation capability to shape itself to the tubular statistics related to geometrical features including tube height, width and length at any arbitrary angle. The introduced boundary analysis in this work provides vectorized and distributed monitoring of tubular changes which requires less complex and smaller convolution kernels, resulting in much lower overall computational cost.

III. DESIGNING DIRECTIONALCONVOLUTIONAL KERNELS

The centerline tracing process is triggered by selecting the initial seed point coordinates in the scala tympani and placing the convolution kernel operators at a specific distance on the tubular borders that act as low-pass differentiators [28] perpendicular to the direction of cochlea as shown in Fig.1. There are four sets of kernels labeled "*right*", "*left*", "*top*" and "*bottom*" placed closely along the initial node of the cochlea and centered on the boundary to identify maximum convolution response. This ensures reduced number of operations per voxel in centerline tracing. The following two features are used in the design of the sampling kernels: 1) the ratio between height and width of a kernel is between

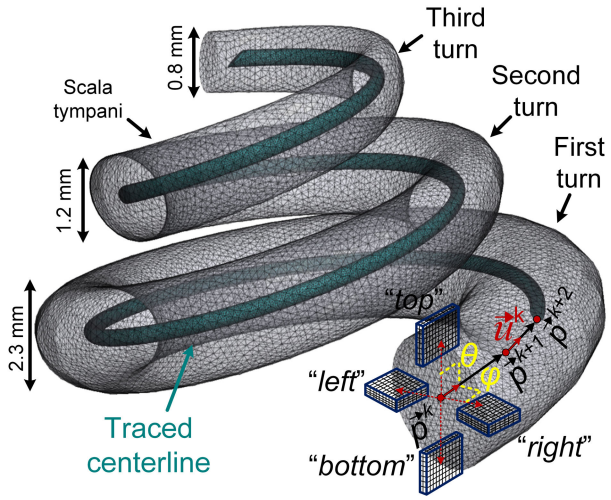

FIGURE 1. Illustrating the 3D tracing algorithm for cochlea application. *"top", "bottom", "right",* and *"left"* kernels are placed on boundary nodes in a relative distance to $\vec{p}^{\,k}$. The kernels are rotated to discretize and compute the convolution responses. The maximum convolution response is used to identify the centerline unit vector optimal angle $\vec{u}_{\sigma}^{\,k}$ that shows the tracing direction from $\vec{p}^{\,k}$ to the next point $\vec{p}^{\,k+1}$. θ and φ show planar discretization around *Z* and *Y* respectively.

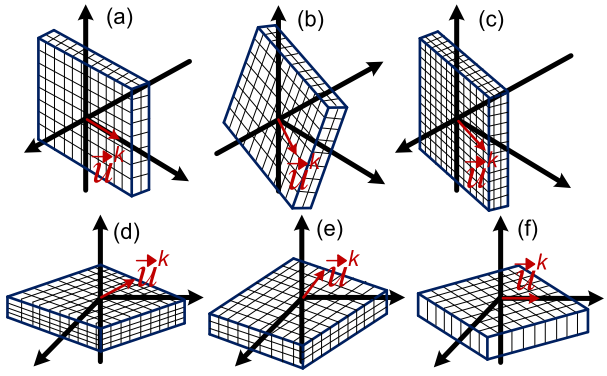

FIGURE 2. Examples of rotated kernels for: (a)-(c) *"top-bottom"* convolutions; (d)-(f) *"right-left"* convolutions. $\vec{u}^{\,k}$ shows the computed convolution on $\vec{p}^{\,k}$. In (b), the angles are indicated by $\vec{u}^{\,k} = [22^{\circ}, 45^{\circ}]$.

2.2 and 2.6 to capture angular variations along the tube; and 2) the kernel length (k) is adjusted adaptively to identify the turning nodes for tracing the highly tortuous structure (Section IV-A).

Let $\vec{u}^{\,k}$ denote a unit vector along the 3D cochlea at point $\vec{p}^{\,k}$. As illustrated in Fig. 1, 3D space directions are indicated by considering two angles, θ and φ around $\vec{u}^{\,k}$; where, θ describes the angular direction around the Z axis and φ describes a rotation around the Y axis after being rotated by θ° around the Z axis. Both θ and φ are discretized to N values each, resulting in a total of N^2 angular directions. The value of N is set to 24 for the most optimal directional convolution resulting in tubular curvature analysis. Therefore, the total number of templates used in directional quantization in the four kernels is $N^2 = 576$. For example, a unit vector along $X(\theta = 0^{\circ}, \varphi = 0^{\circ})$ axis is represented by $\vec{u}^{\,k} = [0, 0]$ as shown in Fig. 2(a). After specifying the unit vector $\vec{u}^{\,k} = [\theta, \varphi]$, the four kernels are correlated recursively with the local image data at pixels starting from $\vec{p}^{\,k}$ along the four directions perpendicular to the $\vec{u}^{\,k} = [\theta, \varphi]$ for identifying the cochlea boundaries.

IV. ALGORITHMS

A. PROPOSED ALGORITHM

1) 3D COCHLEA CENTERLINE TRACING

Let $R = \left[k, \vec{p}^{\,k}, \vec{u}^{\,k}\right]$ denote the convolution response between the image data $I = [x, y, z]$ and the "*right*" kernel where k shows the kernel length in a particular direction $\vec{u}^{\,k}$ from the seed point $\vec{p}^{\,k}$. Similarly, $L = \left[k, \vec{p}^{\,k}, \vec{u}^{\,k}\right]$, $T = \left[k, \vec{p}^{\,k}, \vec{u}^{\,k}\right]$ and $B = \left[k, \vec{p}^{\,k}, \vec{u}^{\,k}\right]$ are convolution responses of the "*left*", "*top*" and "*bottom*" templates respectively. The convolutions are computed through the defined angular steps ($N^2 = 576$) and rotative kernels to sample a series of image locations $I = [x, y, z]$ to identify local boundary analysis. The maximum convolution response identifies the alignment of the kernels to the tube boundaries in a specific direction.

The convolution response (CR) is derived based on a set of low-pass directional differentiators [28] perpendicular to the tube borders:

$$\mathrm{CR} = \sum_{x}^{r}\sum_{y}^{s}\sum_{z}^{t}\begin{pmatrix} I\,[xyz+2]+2I\,[xyz+1] \\ -2I\,[xyz-1]-I\,[xyz-2] \end{pmatrix}/8 \quad (1)$$

where r, s and t define the kernel size. The search for maximum correlation response is limited to $M_1/2$ and $M_2/2$ in each direction at $\vec{p}^{\,k}$. M_1 and M_2 represent the height and width ($M_1 < M_2$) of the reconstructed 3D cochlea model and they vary during the centerline tracing process. This search produces three values at each border including the maximum value of template responses $\{CR_T, CR_B, CR_R$ and $CR_L\}$, local directions at the boundaries $\{u_T, u_B, u_R$ and $u_L\}$ and the distance from centerline at which the maximum response occurs $\{d_T, d_B, d_R$ and $d_L\}$. The aim is to achieve homogeneous convolution responses in the orientations of interest at the "*right*", "*left*", "*top*" and "*bottom*" borders in the tubular structure. However, spatial variations in real cases might cause inconsistency in the resulting convolution values. For simplicity and efficiency, the standard deviation (σ) of $CR_{T,B,R \text{ and } L}$ is proposed as the homogeneity criterion to minimize the effect of unwanted deviations due to localized variations when defining optimal tracing angles. The standard deviation of the maximum convolution responses is:

$$\sigma = \sqrt{\frac{1}{k}\sum_{j=T}^{B,R,L}\left(CR_j - \mu\right)^2}, \quad \mu = \frac{1}{k}\sum_{j=T}^{B,R,L} CR_j \quad (2)$$

where $k = 4$ shows the number of convolution kernels and μ is the median of maximum convolution responses. The optimal tracing angle ($\vec{u}_{\sigma}^{\,k}$) is defined by $CR_{T,B,R \text{ or } L}$ offering the least difference from σ as $argmin \sum_{j=T}^{B,R,L} \left|\sigma - CR_j\right|$. Using the identified optimal tracing angle $\left(\vec{u}_{\sigma}^{\,k}\right)$, the location and direction of the next centerline point is updated as follows:

$$\vec{p}^{\,k+1} = \vec{p}^{\,k} + \alpha\vec{u}_{\sigma}^{\,k} \quad (3)$$

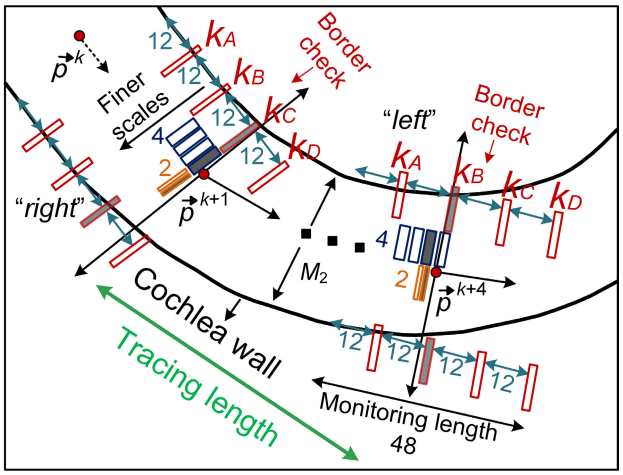

FIGURE 3. Sagittal view of 3D tracing algorithm. Starting from initial point $\vec{p}^{k}$ and tracing angle $\vec{u}_{\sigma}^{k}$, perpendicular nodes (k_A, k_B, k_C, k_D) are searched for monitoring the convolution response changes. The first node satisfying the deviation error condition is picked and divided sequentially into the finer scales to monitor tubular changes and location of $\vec{p}^{k+1}$. As a result, the kernel length is set adaptively and requires low computational cost.

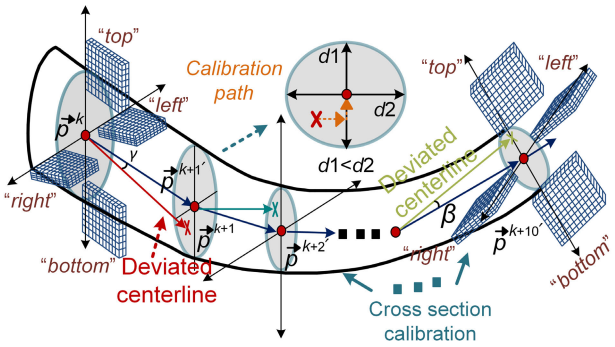

FIGURE 4. Illustrating a segment of 3D cochlea. Cross-section calibration is used to fine-tune the traced centerline coordinates along the segment. Each calibration is shown using a grey circle where the diameters $d1$ and $d2$ are derived using the vectors perpendicular to the vertical-horizontal walls. There is γ° angular error in tracing centerline coordinates from $\vec{p}^{k}$ to $\vec{p}^{k+1}$ which is eliminated using the indicated calibration path.

where α is a step size and is computed according to kernel length (k). Fig. 3 demonstrates that the kernel length (k) is designed to vary adaptively to allow precise tracing of 3D curvatures. This contrasts with [20], which utilizes continuous kernel trajectories at $\vec{u}_{\sigma}^{k}$ for monitoring tubular changes, the proposed discrete and localized border analysis is used to inspect curvatures. This reduces the overall tracing computation cost while retaining high performance. It also favors larger step sizes for straight segments where the longer templates fit well and vice-versa. The initial kernel length is empirically set to 48 samples along the computed tracing angle $\left(\vec{u}_{\sigma}^{k}\right)$. The convolution is computed to identify the angular changes every 12 samples at specific nodes (k_A, k_B, k_C, k_D) as shown in Fig. 3. The node that shows the highest deviation error is then selected and divided sequentially to finer scales [e.g. $12 \rightarrow (3 \times 4)$ and then $4 \rightarrow (2 \times 2)$] to explore accurately the tubular changes. For example, following the steps from $\vec{p}^{k}$ towards $\vec{p}^{k+1}$ in Fig. 3, initial border analysis highlights that the third node (k_C) is the start of the tracing error. The finer scales are illustrated using dark blue and orange rectangles respectively. Note that the proposed border analysis method can be defined as a parametric discrete convolution where the initial length is set to an arbitrary value and the border change investigation is performed using hierarchical coarse-to-fine scales. It is assumed that the convolution value will not be deviated if the tracing angle does not change along the tubular structure. The tracing process is terminated if the convolution responses at each node satisfy the following condition:

$$T_1 < \left(CR_{Tk} + CR_{Bk} + CR_{Lk} + CR_{Rk}\right)/4 < T_2 \qquad (4)$$

where $\{CR_{Tk}, CR_{Bk}, CR_{Rk}, CR_{Lk}\}$ are convolution responses at (k_A, k_B, k_C or k_D); T_1 and T_2 are the sensitivity thresholds for tracing termination determined as a percentage of the maximum convolution response used in identifying $(\vec{u}_{\sigma}^{k})$. As interpreted from the experiments in this work and the simulations in [16], values of thresholds (T) in the range $T_1(=5\%) < T < T_2(=30\%)$ indicate that the tracing algorithm performs reliably. However, low values of T in the range $5\% < T < 15\%$ result in slow tracing and more sensitivity to noise. On the other hand, high values of T in the range $20\% < T < 30\%$ may result in neglecting tortuous tubular changes and premature tracing termination. To achieve a good balance between accuracy and speed of tracing, the average sum of the "*right*", "*left*", "*top*" and "*bottom*" current convolution responses is configured to fall in the range $T_1(=15\%) < T < T_2(=20\%)$.

2) CROSS-SECTION CALIBRATION ENGINE

Two features are derived from cross-section calibration, angular error suppression and monitoring of geometrical variations such as width and height along the cochlea. The proposed calibration engine focuses on localized two-dimensional (2D) cross-section analysis of 3D model before defining the optimal tracing angle $\left(\vec{u}_{\sigma}^{k}\right)$ over $\left(\vec{p}^{k+1} \ldots \vec{p}^{k+n}\right)$ where n shows n$^{\text{th}}$ tracing node as shown in Fig. 4. Cross-section diameters $d1$ and $d2$ are calculated from $\vec{p}^{k+1}$ to the borders by counting the number of pixels along the perpendicular vectors as shown in Fig. 4. The centerpoint coordinates of $d1$ and $d2$ reveal the degree of vertical and horizonal deviations of the traced centerline from the optimal coordinates (defined as the ground truth). The centerline tracing error is due to angular offset accumulation along the tracing step (α), and the calibration unit will correct it by step-by-step elimination. Offset calibration is done either by adding a normalized correction factor $\left(\vec{u}^{k}error\right)$ for negative offsets or subtracting it from the traced centerline coordinate for positive offset values and defined as:

$$\vec{u}^{k}error = \frac{abs\left(\vec{p}^{k+1} - \vec{p}^{k+1'}\right)xyz}{\alpha} \qquad (5)$$

where $\vec{p}^{k+1'}$ shows the corrected seed point. The least deviation occurs at $\vec{p}^{k}$ and has maximum deviation

when it progresses towards the end of the centerline $\vec{p}^{k+1}$. Therefore, the coordinate correction is performed using the following series between start $\vec{p}^{k}$ and end $\vec{p}^{k+1}$ points $\left(1 \times \vec{u}^{k} error, 2 \times \vec{u}^{k} error, \ldots, \alpha \times \vec{u}^{k} error\right)$, mathematically expressed as:

$$Calibrated_{x_i} = \sum_{i=1}^{\alpha} \left(Coordinate_{x_i} \pm i \times \vec{u}^{k} error \right) \quad (6)$$

where $Calibrated_{x_i}$ and $Coordinate_{x_i}$ show the calibrated and uncalibrated values of x coordinates respectively and $\pm$ is used in ascending and descending calibrations. Similarly, the notation for the other two coordinates (y and z) is defined. In addition to the calibration of centerline coordinates, $d1$ and $d2$ are also used to monitor the horizontal and vertical width variations in cochlea centerline tracing. The placement of "*right*", "*left*", "*top*" and "*bottom*" convolution kernel engines are based on captured tubular border locations from $d1$ and $d2$. After correcting the centerline coordinates, the convolution kernels are rotated to identify the next tracing angle. Since the tubular changes are limited, the next tracing angle search is carried within a small number of directions, denoted by Ψ, that are adjacent to $\vec{u}_{\sigma}^{k}$:

$$\Psi = \left\{ \vec{u}_{\sigma}^{k} + (\pm\zeta_1, \pm\zeta_2 \right\}, \quad \left| \zeta_1, \zeta_2 = \Delta_{\theta,\varphi} \right| \quad (7)$$

where $\Delta_{\theta,\varphi}$ is the maximum number of neighboring directions and can be set either manually or adaptively through estimation of noise level. The typical value of $\Delta_{\theta,\varphi}$ is empirically set to $\Delta_{\theta,\varphi}$= 20; therefore the number of computations for identifying the next tracing angle is reduced substantially from 576 to 28 directions. The proposed algorithm is referred to as Supercylinder for the rest of the paper.

B. OTHER TRACING ALGORITHMS FOR COMPARISON

1) 3D CYLINDER [20]

This is a rapid and fully automatic 3D tracing algorithm which utilizes directional kernels to identify the neuronal topology, guided by a generalized 3D cylinder model with elliptical cross sections. Starting from a seed point $\vec{p}^{k}$, four kernels perpendicular to the tube are exploited in a 3D cylinder, to discretize the possible angular orientations. The orientations of the kernels that produce the maximum response yield an initial estimate of the tracing direction $\vec{u}^{k}$ that is used in tracing the tubular structure by predicting the centerline points $\left(\vec{p}^{k}, \vec{p}^{k+1} \ldots \vec{p}^{k+S}\right)$, where S is the tracing length. A variable-length continuous template is employed to identify S at each iteration.

2) FRANGI VESSELNESS [12], [29]–[31]

Frangi vesselness is based on local shape descriptors or tube detection filters. It uses multiscale tube detection filters to construct a representation of tubular objects of different sizes at different scales. The tubes are filtered with bottom-up local shape descriptors or tube detection filters based on an eigenvalue analysis of the Hessian matrix (H) [12]. It is capable of coping with anisotropic voxels with varying widths. The eigenvalues of H are represented by λ_1, λ_2 and λ_3 where $\lambda_1 < \lambda_2 < \lambda_3$. Their corresponding normalized eigenvectors are $\vec{v_1}$, $\vec{v_2}$, and $\vec{v_3}$; $\vec{v_1}$ provides the tube direction, $\vec{v_2}$ and $\vec{v_3}$ represent the tube cross-section vectors. The tube cross-section is constructed along a 2D plane using the vesselness function (U) and the derived eigenvectors. Thus, Frangi vesselness provides both the centerline coordinates and the radius of the tube. Frangi vesselness is a powerful multiscale filter for identifying tubular objects but designing the filtering scales to capture the tubular changes is a tedious task and overall it requires extensive computational costs.

3) ACTIVE CONTOUR [32]–[35]

Active contour is a region growing algorithm represented by a parametrized surface that deforms through the structure of interest in volume. Its evolution is driven by internal and external forces that act on the contour in specific directions. Active contour uses different approaches to define internal and external forces, i.e. deriving the external force from the gradient magnitude of image intensity [36]. A notorious problem with using Active contour is initialization. In general, the starting contour must be close to the true boundary otherwise it is likely to converge at the wrong point [37]. However, in tracing the cochlea centerline the difficulty of initialization is addressed by having access to the initial seed point in the scala tympani. Active contour in this work uses the minimization of energy function through solving Euler equations and the iterative numerical method in [37]. The major disadvantage of Active contour is that the limited use of structural information in the deformation iterations might lead to a high chance of leakage. In addition, iterative modifying of the contour is complex and very time consuming.

V. RESULTS AND VALIDATION

The tracing algorithms were applied to a set of three images: one synthetic cochlea (Model 1) and two real cochlea models constructed from micro-CT [38] images (Model 2 and Model 3). The purpose of utilizing synthetic data is to provide an analysis of the algorithms under controlled conditions that mimic the cochlea structure. The synthetic model used for centerline tracing validation was made by the following expressions:

$$x = \left(\frac{s}{5}\right) \sin(s), \quad y = \left(\frac{s}{5}\right) \cos(s), \quad z = \left(-\frac{s}{3}\right) \quad (8)$$

where s ranges from 6.5 to 21.25 to resemble the anatomical human cochlea with a mean length and diameter of 41.5 mm and 2 mm respectively [5]. The synthetic 3D cochlea was for a 10 mm × 10 mm × 10 mm volume comprising the cochlea model and the pad arrays to obtain consistent (x, y, z) dimensions for examination of tracing performance. Model 2 and Model 3 evaluate the centerline tracing algorithm against the "golden standard," i.e., a hand-traced centerline by clinicians in realistic reconstructed cochlea models. The realistic cochlea models were reconstructed using micro-CT images of 512 × 512 pixels per slice databases from the

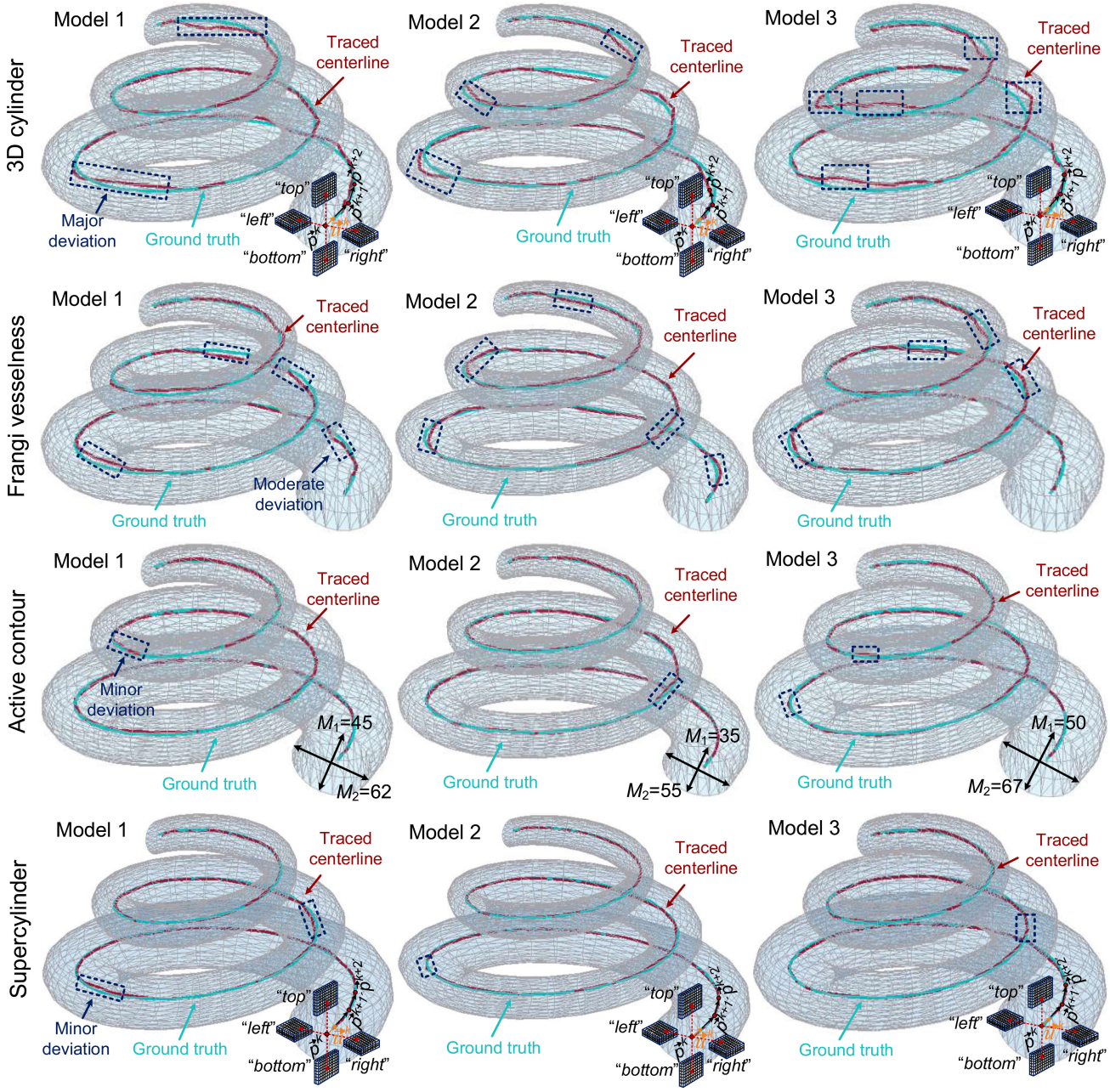

FIGURE 5. Automated tracing along a 3D cochlea. The columns represent three cochlea models including one synthetic (Model 1) and two real models (Model 2 and Model 3) for centerline tracing visualization. The rows, from top to bottom, show the tracing algorithms utilized to detect centerline coordinates: 3D cylinder [20], Frangi vesselness [12], [29]–[31], Active contour [32]–[35] and Supercylinder. The ground truth and traced centerline coordinates are shown in cyan and red colors respectively in each model. The figure also identifies dotted rectangles at different regions for visual assessment of deviations (i.e. minor, moderate, and major) in centerline tracing. Evaluation of the traced centerline coordinates $\left(\tilde{p}^{k}, \tilde{p}^{k+1'} \ldots \tilde{p}^{k+n'}\right)$ to the ground-truth also shows there is less than 6 pixels deviation error in the calibrated centerline coordinates in the proposed algorithm.

Royal National Throat, Nose and Ear Hospital, and a manually defined ground-truth was used to quantify traversal performance [39].

Fig. 5 shows the 3D cochlea models, their corresponding ground truth and the traced centerline coordinates. The rows are associated with the 3D cylinder, Frangi vesselness, Active contour and Supercylinder algorithms. In each example dotted rectangles are superimposed on the 3D cochlea models in appropriate regions to highlight minor, moderate and major deviations. The first row in Fig. 5 shows that the 3D cylinder does not perform reliably when it is faced with high-order tubular changes, especially in cochlea models with complex geometrical variations. In the second row, Frangi vesselness has moderate deviations in tracing the centerline coordinates. In the third row the traced centerline coordinates using Active contour shows a similar performance to Supercylinder. The disadvantage of Frangi vesselness and Active contour is that they are applied to the whole 3D volumes and 3D structures

TABLE 1. Processing time in seconds taken for centerline extraction using different algorithms.

Cochlea model	Processing time (seconds)			
	Frangi vesselness	Active contour	3D cylinder	Supercylinder
Model 1	161	102	9.8	7.9
Model 2	120	87	12.4	6.9
Model 3	261	121	10.5	9.4
Model 4	114	76	7.3	5.8
Model 5	167	93	10.86	8.2
Model 6	139	79	9.39	7.6
Model 7	233	108	13.56	9.1
Model 8	125	77	7.1	6.2

to detect the centerline coordinates which is not suited to real-time surgical procedures. In each tracing trial, centerline coordinates are recorded and compared with the ground truth. The traced centerline coordinates present the optimal path for surgical purposes as studied in [39], [40], where an impedance model estimates the proximity of an inserted surgical electrode array to the cochlea wall.

A. PROCESSING TIME

A standard and reliable technique to obtain the computational cost of tracing algorithms is to derive the execution time which effectively correlates with the number of arithmetic operations (i.e. number of additions (or subtractions) and the number of multiplications (or divisions)) per voxel. For example, in the Supercylinder the arithmetic operations are related to identifying the optimal tracing angle ($\vec{u}_\sigma^k$), the discrete border analysis to monitor tubular changes, and the cross-section calibration engine to readjust the centerline coordinates.

All 3D cochlea models used in visualization (Models 1, 2, 3) and also five additional generated 3D cochlea models (Models 4, …,8) were traced using Matlab on a PC with 2 GHz Intel Core i7 processor, and 128 Mbytes of RAM. The constructed models (Models 1, …,8) represent height and width ($M_1 < M_2$) variations in human cochlea anatomy.

Table 1 shows the processing time required for centerline extraction by Frangi vesselness, Active contour, 3D cylinder and Supercylinder. Supercylinder is on average around 21.6 times faster than Frangi vesselness, 12.2 times faster than Active contour and 1.3 times faster than 3D cylinder. The main reason for the reduction of the execution time in Supercylinder is the application of sparse voxel processing to reduce the overall tracing cost. As shown in the last column of Table 1, the average computed tracing time for the cochlea models (Models 1, …, 8) comprising ($650 \times 650 \times 650$) pixels with pad arrays, is 7.6 seconds. For a 16 electrode cochlear implant array [41], each insertion step on average requires about 480 ms computation suggesting that Supercylinder is suitable for realizing accurate real-time cochlear guidance surgery. Note that $\cong 40\%$ of the overall tracing time is used to identify the first cochlea segment tracing angle ($\vec{u}_\sigma^k$) as a result of the number of rotated kernels employed in directional quantization $N^2 = 576$.

TABLE 2. Tracing perfomance analysis.

	Model 1	Model 2	Model 3
Overall traced length (pixels)	486	486	486
Initial height-width (M_1-M_2)	45-62	35-55	50-67
Tracing time (seconds)	7.9	6.9	9.4
TTP - 3D cylinder	312	263	213
FTP - 3D cylinder	174	223	273
CDR - 3D cylinder	64.1%	54.1%	43.8%
TTP - Frangi vesselness	413	395	431
FTP - Frangi vesselness	73	91	55
CDR - Frangi vesselness	84.9%	81.2%	88.6%
TTP - Active contour	458	439	466
FTP - Active contour	28	47	20
CDR - Active contour	94.2%	90.3%	95.8%
TTP - Supercylinder	450	463	443
FTP - Supercylinder	36	23	43
CDR - Supercylinder	92.5%	95.2%	91.1%

* Overall tracing performance of 3D cylinder, Frangi vesselness and Active contour are 54%, 84.9% and 93.4% respectively.

B. TRACING PERFORMANCE EVALUATION

This section highlights the important criteria for quantitative evaluation of tracing performance. The first criterion is the centerline detection ratio (CDR) which is used to distinguish between the tracing proficiency exploiting the ground-truth and the traced centerline coordinates. It is defined as:

$$\text{CDR} = \frac{\text{TTP}}{\text{TTP} + \text{FTP}} \times 100\% \tag{9}$$

where TTP is the number of true traced pixels and FTP the false traced pixels due to random noise or artefacts.

Table 2 compares the CDR performance of Supercylinder and the other tracing algorithms discussed in Section IV. It demonstrates the CDR performance superiority of Supercylinder using the variable geometrical complexities embedded in Model l, Model 2 and Model 3. Averaging the CDR yields 92.9% tracing performance (i.e. maximum tracing error is below 6 pixels) on cochlea models for Supercylinder compared to 54% for 3D cylinder which highlights its sensitivity to geometrical complexities. The overall CDR difference between Supercylinder and Frangi vesselness is 8% with 21.6× lower execution time. Table 2 also shows that Supercylinder produces almost the same total average CDR compared with Active contour on different cochlea models.

The second criterion is the measured tracing performance with varying degrees of noise added to each cochlea model. The assessment procedure in noisy conditions estimates and records the mean-squared-error (MSE) of the traced coordinates (Tr) to the ground truth (Gr). In each noisy trial:

$$\text{MSE} = \frac{1}{Le} \sum_{i=0}^{Le-1} (Tr_i - Gr_i)^2 \tag{10}$$

where Le is the tracing length. Fig. 6 (a)-(c) show the calculated MSE as a function of noise for the synthetic (Model 1) and two real cochlea models (Model 2 and Model3).

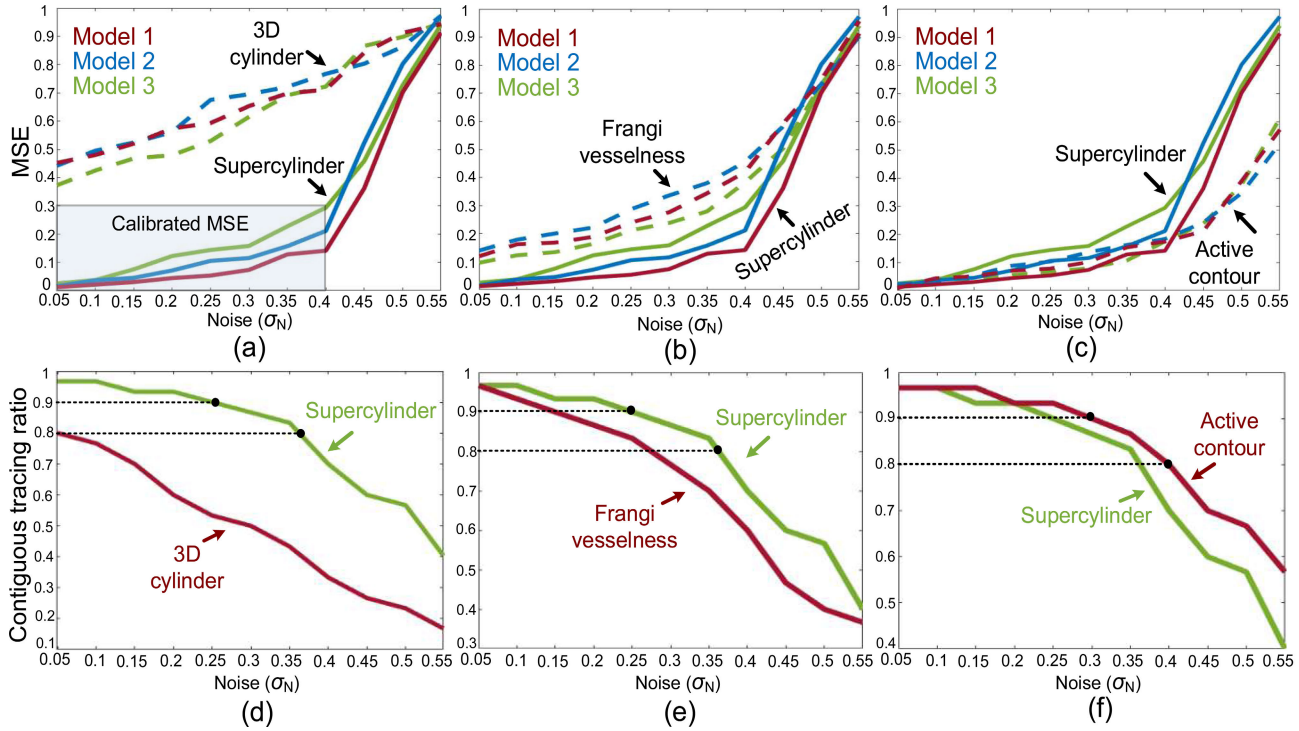

FIGURE 6. (a)-(c) The calculated MSE in the centerline coordinates to the ground truth as a function of noise compiled for the synthetics (Model 1) and two real cochlea models (Model 2 and Model3). (a)-(c) also compare the MSE of Supercylinder to 3D cylinder [20], Frangi vesselness [12], [29]–[31] and Active contour [32]–[35]. Note that the MSE in the calibration zone of the Supercylinder algorithm is within approximately 10 pixels to the ground truth except noise level $\sigma_N > 0.4$ where MSE rises rapidly. Frangi vesselness and Active contour maintain low MSE at increasing noise levels. (d)-(f) Show the ratio of successful iterations completed by Supercylinder as a function of noise compared with 3D cylinder, Frangi vesselness and Active contour.

Typically, the added noise corrupts the decision-making process in defining optimal tracing angle ($\vec{u}_\sigma^k$) and this results in either minor or major deviations from the ground truth (i.e. the safe surgery path). The results in Fig. 6(a) show that for $\sigma_N < 0.4$, the average MSE of the three models for Supercylinder is below 0.3 (i.e. approximately 10 pixels) compared with 0.4 to 0.7 for 3D cylinder. For $\sigma_N > 0.4$ the MSE of Supercylinder increases rapidly. Fig. 6(b) shows that for Frangi vesselness the average MSE is below 0.4 for $\sigma_N < 0.4$ and increases immediately for $\sigma_N > 0.4$. Fig. 6(c) also shows that for both Supercylinder and Active contour, MSE increases linearly up to $\sigma_N = 0.4$, and for $\sigma_N > 0.4$ the MSE of Active contour outperforms Supercylinder in all cochlea models.

Next, the ability of the four algorithms to generate smooth and contiguous traces under noisy conditions is examined. The ratio of successful trials in tracing centerlines in all trials is calculated and shown in Fig. 6 (d)-(f). The graphs are computed from a total of 90 trials for all three cochlea models (30 trials per model). Note that at ($0.05 < \sigma_N < 0.4$) in Fig. 6(d), all tested models are traversed contiguously because of the decision-making process [Eq. (2)] and the calibration unit which successfully corrects the unwanted deviations due to embedded noise in the Supercylinder algorithm. In Fig. 6(f), the ratio of successfully traced centerline coordinates by Active contour algorithm are higher compared to Supercylinder but has 12.2× longer execution time.

VI. CONCLUSION AND DISCUSSION

A novel algorithm (Supercylinder) has been presented that automatically tracks 3D tubular structures (e.g. cochlea model) without the need of user intervention. Supercylinder comprises three main blocks: 1) angular border analysis, 2) discrete and adaptive kernels for identifying the tracing jump and 3) utilization of a calibration engine. The calibration engine as part of Supercylinder performs cross-section tuning of identified coordinates to the "*right*", "*left*", "*top*" and "*bottom*" borders before establishing the next tubular segment optimal tracing angle $(\vec{u}_\sigma^k)$. Supercylinder has been tested on three 3D cochlea models. One was a synthetic image and two were constructed based on real models. Using these datasets, Supercylinder was validated for centerline accuracy, noise robustness analysis, and processing time to demonstrate its key strengths. The results confirm reliable 3D tracing with an average CDR of 92.9%. Supercylinder has a low MSE in the presence of noise. The contingency test showed that the number of successful tracing completed over 90 trials is over 0.8 (or 80%) for the noise limits $0.05 < \sigma_N < 0.4$.

Other tracing algorithms including 3D cylinder, Frangi vesselness and Active contour were also implemented for comparison. In terms of processing time, only 3D cylinder competes with Supercylinder but it provides poor tracing performance. Compared with Active contour, Supercylinder avoids high computational cost and has similar CDR and MSE performance. Amongst the implemented algorithms,

Active contour shows superior noise immunity even for $\sigma_N > 0.4$. Supercylinder experiences minor deviations when tracing the centerline coordinates and this issue is aggravated when the noise is superimposed on the tube border. This is due to the uncertainty when placing the tracing kernels to estimate the optimal tracing angle ($\vec{u}_\sigma^k$). In future designs, this issue can be mitigated if the cross-section calibration engine is incorporated with an enhancement filter to generate a smooth cross-section structure. This aids the accurate identification of where the locations of the convolution kernels are placed to estimate $\vec{u}_\sigma^k$ and consequently enhancing the noise robustness. Design and implementation of a highly efficient CNN to address both reliability and prevention of excessive computations applicable to real-time surgical set-ups is another approach that can increase the noise robustness considerably. The Supercylinder tracing algorithm will eventually be integrated into an online surgical guide for safe insertion of cochlear implant electrode arrays.

REFERENCES

[1] F.-G. Zeng, S. Rebscher, W. Harrison, X. Sun, and H. Feng, "Cochlear implants: System design, integration, and evaluation," *IEEE Rev. Biomed. Eng.*, vol. 1, pp. 115–142, Jan. 2008.

[2] B. S. Wilson and M. F. Dorman, "Cochlear implants: A remarkable past and a brilliant future," *Hearing Res.*, vol. 242, nos. 1–2, pp. 3–21, Aug. 2008.

[3] J. Wouters, H. J. McDermott, and T. Francart, "Sound coding in cochlear implants: From electric pulses to hearing," *IEEE Signal Process. Mag.*, vol. 32, no. 2, pp. 67–80, Mar. 2015.

[4] T. Moser and A. Starr, "Auditory neuropathy—Neural and synaptic mechanisms," *Nature Rev. Neurol.*, vol. 12, no. 3, pp. 135–149, Mar. 2016.

[5] E. Erixon, H. Högstorp, K. Wadin, and H. Rask-Andersen, "Variational anatomy of the human cochlea: Implications for cochlear implantation," *Otology Neurotol.*, vol. 30, no. 1, pp. 14–22, Jan. 2009.

[6] L. Adams, W. Krybus, D. Meyer-Ebrecht, R. Rueger, J. M. Gilsbach, R. Moesges, and G. Schloendorff, "Computer-assisted surgery," *IEEE Comput. Graph. Appl.*, vol. 10, no. 3, pp. 43–51, May 1990.

[7] A. Rodriguez, D. B. Ehlenberger, D. L. Dickstein, P. R. Hof, and S. L. Wearne, "Automated three-dimensional detection and shape classification of dendritic spines from fluorescence microscopy images," *PLoS ONE*, vol. 3, no. 4, p. e1997, Apr. 2008.

[8] B. Al-Diri, A. Hunter, and D. Steel, "An active contour model for segmenting and measuring retinal vessels," *IEEE Trans. Med. Imag.*, vol. 28, no. 9, pp. 1488–1497, Sep. 2009.

[9] A. M. Mendonca and A. Campilho, "Segmentation of retinal blood vessels by combining the detection of centerlines and morphological reconstruction," *IEEE Trans. Med. Imag.*, vol. 25, no. 9, pp. 1200–1213, Sep. 2006.

[10] M. Sofka and C. V. Stewart, "Retinal vessel centerline extraction using multiscale matched filters, confidence and edge measures," *IEEE Trans. Med. Imag.*, vol. 25, no. 12, pp. 1531–1546, Dec. 2006.

[11] M. Erdt, M. Raspe, and M. Suehling, "Automatic hepatic vessel segmentation using graphics hardware," in *Medical Imaging and Augmented Reality* (Lecture Notes in Computer Science), vol. 5128. Berlin, Germany: Springer, 2008, pp. 403–412.

[12] A. Frangi, W. Niessen, K. L. Vincken, and M. A. Viergever, "Multiscale vessel enhancement filtering," in *Proc. MICCAI*, 1998, pp. 130–137.

[13] O. Friman, M. Hindennach, C. Kühnel, and H.-O. Peitgen, "Multiple hypothesis template tracking of small 3D vessel structures," *Med. Image Anal.*, vol. 14, no. 2, pp. 160–171, Apr. 2010.

[14] M. M. G. Macedo, C. Mekkaoui, and M. Jackowski, I. Bloch and R. M. Cesar, Eds., "Vessel centerline tracking in CTA and MRA images using Hough transform," in *Proc. CIARP*, in Lecture Notes in Computer Science, vol. 6419. Berlin, Germany: Springer, 2010, pp. 295–302. [Online]. Available: https://link.springer.com/chapter/10.1007%2F978-3-642-16687-7_41#citeas

[15] J. A. Tyrrell, E. di Tomaso, D. Fuja, R. Tong, K. Kozak, R. K. Jain, and B. Roysam, "Robust 3-D modeling of vasculature imagery using superellipsoids," *IEEE Trans. Med. Imag.*, vol. 26, no. 2, pp. 223–237, Feb. 2007.

[16] A. Can, H. Shen, J. N. Turner, H. L. Tanenbaum, and B. Roysam, "Rapid automated tracing and feature extraction from retinal fundus images using direct exploratory algorithms," *IEEE Trans. Inf. Technol. Biomed.*, vol. 3, no. 2, pp. 125–138, Jun. 1999.

[17] H. Shen, B. Roysam, C. V. Stewart, J. N. Turner, and H. L. Tanenbaum, "Optimal scheduling of tracing computations for real-time vascular landmark extraction from retinal fundus images," *IEEE Trans. Inf. Technol. Biomed.*, vol. 5, no. 1, pp. 77–91, Mar. 2001.

[18] G. Lin, C. V. Stewart, B. Roysam, K. Fritzsche, G. Yang, and H. L. Tanenbaum, "Predictive scheduling algorithms for real-time feature extraction and spatial referencing: Application to retinal image sequences," *IEEE Trans. Biomed. Eng.*, vol. 51, no. 1, pp. 115–125, Jan. 2004.

[19] C.-L. Tsai, C. V. Stewart, H. L. Tanenbaum, and B. Roysam, "Model-based method for improving the accuracy and repeatability of estimating vascular bifurcations and crossovers from retinal fundus images," *IEEE Trans. Inf. Technol. Biomed.*, vol. 8, no. 2, pp. 122–130, Jun. 2004.

[20] K. A. Al-Kofahi, S. Lasek, D. H. Szarowski, C. J. Pace, G. Nagy, J. N. Turner, and B. Roysam, "Rapid automated three-dimensional tracing of neurons from confocal image stacks," *IEEE Trans. Inf. Technol. Biomed.*, vol. 6, no. 2, pp. 171–187, Jun. 2002.

[21] M. Schneider, S. Hirsch, B. Weber, G. Székely, and B. H. Menze, "Joint 3-D vessel segmentation and centerline extraction using oblique Hough forests with steerable filters," *Med. Image Anal.*, vol. 19, no. 1, pp. 220–249, Jan. 2015.

[22] A. Sironi, E. Turetken, V. Lepetit, and P. Fua, "Multiscale centerline detection," *IEEE Trans. Pattern Anal. Mach. Intell.*, vol. 38, no. 7, pp. 1327–1341, Jul. 2016.

[23] M. A. Gülsün, G. Funka-Lea, P. Sharma, S. Rapaka, and Y. Zheng, "Coronary centerline extraction via optimal flow paths and CNN path pruning," in *Proc. MICCAI*, Athens, Greece, 2016, pp. 317–325.

[24] J. M. Wolterink, R. W. van Hamersvelt, M. A. Viergever, T. Leiner, and I. Išgum, "Coronary artery centerline extraction in cardiac CT angiography using a CNN-based orientation classifier," *Med. Image Anal.*, vol. 51, pp. 46–60, Jan. 2019.

[25] L. Yu, J.-Z. Cheng, Q. Dou, X. Yang, H. Chen, J. Qin, and P.-A. Heng, "Automatic 3D cardiovascular MR segmentation with densely-connected volumetric convnets," in *Proc. MICCAI*, Quebec City, QC, Canada, 2017, pp. 287–295.

[26] B. Kong, X. Wang, J. Bai, Y. Lu, F. Gao, K. Cao, J. Xia, Q. Song, and Y. Yin, "Learning tree-structured representation for 3D coronary artery segmentation," *Comput. Med. Imag. Graph.*, vol. 80, Mar. 2020, Art. no. 101688.

[27] F. Yu and V. Koltun, "Multi-scale context aggregation by dilated convolutions," 2015, *arXiv:1511.07122*. [Online]. Available: http://arxiv.org/abs/1511.07122

[28] Y. Sun, R. J. Lucariello, and S. A. Chiaramida, "Directional low-pass filtering for improved accuracy and reproducibility of stenosis quantification in coronary arteriograms," *IEEE Trans. Med. Imag.*, vol. 14, no. 2, pp. 242–248, Jun. 1995.

[29] G. Yang, P. Kitslaar, M. Frenay, A. Broersen, M. J. Boogers, J. J. Bax, J. H. C. Reiber, and J. Dijkstra, "Automatic centerline extraction of coronary arteries in coronary computed tomographic angiography," *Int. J. Cardiovascular Imag.*, vol. 28, no. 4, pp. 921–933, Apr. 2012.

[30] K. Krissian, G. Malandain, N. Ayache, R. Vaillant, and Y. Trousset, "Model-based detection of tubular structures in 3D images," *Comput. Vis. Image Understand.*, vol. 80, no. 2, pp. 130–171, Nov. 2000.

[31] R. P. Kumar, F. Albergtsen, M. Reimers, T. Langø, B. Edwin, and O. J. Elle, "3D multiscale vessel enhancement based centerline extraction of blood vessels," in *Proc. SPIE Med. Imag.*, Lake Buena Vista, FL, USA, 2013, Art. no. 86691X.

[32] Y. Wang, A. Narayanaswamy, C.-L. Tsai, and B. Roysam, "A broadly applicable 3-D neuron tracing method based on open-curve snake," *Neuroinformatics*, vol. 9, nos. 2–3, pp. 193–217, Sep. 2011.

[33] P. A. Yushkevich, J. Piven, H. C. Hazlett, R. G. Smith, S. Ho, J. C. Gee, and G. Gerig, "User-guided 3D active contour segmentation of anatomical structures: Significantly improved efficiency and reliability," *NeuroImage*, vol. 31, no. 3, pp. 1116–1128, Jul. 2006.

[34] B. Li and S. T. Acton, "Active contour external force using vector field convolution for image segmentation," *IEEE Trans. Image Process.*, vol. 16, no. 8, pp. 2096–2106, Aug. 2007.

[35] D. Wu, D. Liu, Z. Puskas, C. Lu, A. Wimmer, C. Tietjen, G. Soza, S. K. Zhou, "A learning based deformable template matching method for automatic rib centerline extraction and labeling in CT images," in *Proc. CVPR*, Providence, RI, USA, Jun. 2012, pp. 980–987.
[36] V. Caselles, R. Kimmel, and G. Sapiro, "On geodesic active contours," *Int. J. Comput. Vis.*, vol. 22, no. 1, pp. 61–79, 1997.
[37] C. Xu and J. L. Prince, "Snakes, shapes, and gradient vector flow," *IEEE Trans. Image Process.*, vol. 7, no. 3, pp. 359–369, Mar. 1998.
[38] S. R. Stock, *Microcomputed Tomography: Methodology and Applications*. Boca Raton, FL, USA: CRC Press, 2008.
[39] E. Salkim, M. Zamani, D. Jiang, and A. Demosthenous, "Detection of electrode array proximity to cochlea wall based on impedance variation: Computational study," in *Proc. IEEE Conf. Modelling and Simulation (UKSIM)*, Cambridge, U.K., Mar. 2020, pp. 1–4.
[40] C. K. Giardina, E. S. Krause, K. Koka, and D. C. Fitzpatrick, "Impedance measures during *in vitro* cochlear implantation predict array positioning," *IEEE Trans. Biomed. Eng.*, vol. 65, no. 2, pp. 327–335, Feb. 2018.
[41] A. Dhanasingh and C. Jolly, "An overview of cochlear implant electrode array designs," *Hearing Res.*, vol. 356, pp. 93–103, Dec. 2017.

MAJID ZAMANI (Member, IEEE) was born in Tehran, Iran, in 1984. He received the M.Sc. degree in microelectronics from Islamic Azad University, Science and Research Branch, Tehran, in 2011, and the Ph.D. degree from University College London (UCL), London, U.K., in 2017. He is currently a Research Associate with the Analog and Biomedical Electronics Group, UCL. His research interests include design and fabrication of advanced and energy-efficient computational systems utilizing pattern recognition, machine learning, and computer vision algorithms, especially for wearable and implantable biomedical applications. He was recipient of the Overseas Research Scholarship and the UCL Graduate Research Scholarship to pursue his Ph.D. degree. He was also a recipient of the Best Researcher M.Sc. Student Award.

ENVER SALKIM (Member, IEEE) received the B.S. degree (Hons.) in electrical and electronic engineering from Karadeniz Technical University, Trabzon, Turkey, in 2012, the M.Sc. degree in advanced electronics engineering from Brunel University London, London, U.K., in 2014, and the Ph.D. degree from University College London (UCL), London, in 2019. He is currently a Research Associate with the Analog and Biomedical Electronics Group. His research interests include the design and development of medical devices using bio-computational modeling and circuit design for wearable and implantable applications. He was a recipient of the Turkish Government Scholarship to pursue his M.Sc. and Ph.D. degrees.

SHAKEEL R. SAEED received the M.B.B.S. degree from King's College London, London, U.K., in 1985, and the M.D. degree from The University of Manchester, Manchester, U.K., in 2003. He is currently a Professor of otology/neuro-otology with the Ear Institute, University College London, and the Consultant ENT and Skull Base Surgeon of the Royal National Throat, Nose and Ear Hospital, and the National Hospital for Neurology and Neurosurgery, London. He has extensive experience in lateral skull base surgery and implantation otology leading U.K. opinion in this field. He has performed over 2000 complex ear surgeries, over 400 cochlear implant surgeries, over 500 vestibular schwannoma (acoustic neuroma) and other skull base surgeries, and over 25 auditory brainstem implant surgeries (adults and children). He is active in otological research and peer review and has over 100 peer-reviewed publications, and over 250 presentations and scientific meetings. He is a Principal Investigator on a range of clinical trials as part of his commitment to seek solutions to the challenging ear problems his patients face.

ANDREAS DEMOSTHENOUS (Fellow, IEEE) received the B.Eng. degree in electrical and electronic engineering from the University of Leicester, Leicester, U.K., in 1992, the M.Sc. degree in telecommunications technology from Aston University, Birmingham, U.K., in 1994, and the Ph.D. degree in electronic and electrical engineering from University College London (UCL), London, U.K., in 1998.

He is currently a Professor with the Department of Electronic and Electrical Engineering, UCL, and leads the Analog and Biomedical Electronics Group. He has made outstanding contributions to improving safety and performance in integrated circuit design for active medical devices, such as spinal cord and brain stimulators. He has numerous collaborations for cross-disciplinary research, both within the U.K. and internationally. He has authored over 300 articles in journals and international conference proceedings, several book chapters, and holds several patents. His research interests include analog and mixed-signal integrated circuits for biomedical, sensor, and signal processing applications. He is a Fellow of the Institution of Engineering and Technology and a Chartered Engineer. He was a co-recipient of a number of Best Paper Awards and has graduated many Ph.D. students. He has served on the technical committees for a number of international conferences, including the European Solid-State Circuits Conference (ESSCIRC) and the International Symposium on Circuits and Systems (ISCAS). He was an Associate Editor (from 2006 to 2007) and the Deputy Editor-in-Chief (from 2014 to 2015) of the IEEE TRANSACTIONS ON CIRCUITS AND SYSTEMS—II: EXPRESS BRIEFS and an Associate Editor (from 2008 to 2009) and the Editor-in-Chief (from 2016 to 2019) of the IEEE TRANSACTIONS ON CIRCUITS AND SYSTEMS—I: REGULAR PAPERS. He is an Associate Editor of the IEEE TRANSACTIONS ON BIOMEDICAL CIRCUITS AND SYSTEMS and serves on the International Advisory Board of *Physiological Measurement*.